Journal Pre-proof

Methodology for parameter identification on a thermoplastic composite crash absorber by the Sequential Response Surface Method and Efficient Global Optimization

Elena Raponi, Dario Fiumarella, Simonetta Boria, Alessandro Scattina, Giovanni Belingardi

PII: S0263-8223(21)01105-3
DOI: https://doi.org/10.1016/j.compstruct.2021.114646
Reference: COST 114646

To appear in: *Composite Structures*

Received date : 21 July 2021
Revised date : 18 August 2021
Accepted date : 4 September 2021

Please cite this article as: E. Raponi, D. Fiumarella, S. Boria et al., Methodology for parameter identification on a thermoplastic composite crash absorber by the Sequential Response Surface Method and Efficient Global Optimization. *Composite Structures* (2021), doi: https://doi.org/10.1016/j.compstruct.2021.114646.

Methodology for Parameter Identification on a Thermoplastic Composite Crash Absorber by the Sequential Response Surface Method and Efficient Global Optimization

Elena Raponi[a,*], Dario Fiumarella[b], Simonetta Boria[a], Alessandro Scattina[b], Giovanni Belingardi[b]

[a]*School of Sciences and Technology, Mathematics division, University of Camerino, Via Madonna delle Carceri 9, 62032 Camerino, Italy*
[b]*Department of Mechanical and Aerospace Engineering, Politecnico di Torino, Corso Duca degli Abruzzi 24, 10129 Torino, Italy*

Abstract

Numerical simulations for crashworthiness require the definition of material properties that are not always predictable with standard experimental tests. This paper deals with the numerical optimization of a thermoplastic composite material model. The component is a vehicle impact attenuator made of an innovative All-PP (PolyPropylene) composite material. The peculiar failure mechanism of this material makes the numerical simulation of the collapse a difficult challenge to achieve with a trial-and-error calibration of the material card. Therefore, an optimization procedure is proposed to determine the material parameters. The optimization is implemented in LS-OPT, where the mean square error between the experimental and numerical load-displacement curves is the objective function to be minimized. Two test cases are considered: (1) optimization of the material card based on the full load-displacement curve from the experimental tests and (2) optimization of relevant parameters of a numerical trigger added to control initial contact instabilities between the impacting rigid wall and the component in the numerical simulations. The optimization strategies Sequential Response Surface Method (SRSM) and Efficient Global Optimization (EGO) are used. The results show that the presented methodology allows characterizing the studied composite material and thus obtaining a more efficient numerical model.

Keywords: Crashworthiness, Composite impact attenuator, Finite element analysis, Efficient Global Optimization, Sequential Response Surface Method, Surrogate models

1. Introduction

In recent years, fiber reinforced thermoplastic (FRTP) composites have been increasingly attracting the attention of automotive manufacturers [1]. The demand for the development of FRTP composites arise from the need to respect the always more strict environmental regulations in terms of CO_2, waste recover, reuse and recyclability. Several studies on the recyclability of thermoplastic materials and FRTP composites [2–8] demonstrate the advantages of this class of materials due to the possibility of reuse or recovery of fibers or matrix at the end of the life cycle of the components. In addition to recyclability, FRTP composites are of great interest due to their peculiar mechanical properties and high damage tolerance compared to conventional fiber reinforced thermoset (FRTS) composites [9–16]. In terms of automotive application, crashworthiness is one of the most important aspects to be considered. It refers to the ability of a component to absorb energy during an impact event. Conventional FRTS composites exhibit good energy absorption properties in addition to their light weight and strength. However, compared to FRTS composites, FRTP composites generally respond differently to a crush loading, with the interplay of multiple failure modes, such as delamination, matrix cracking, matrix-fiber debonding, and fiber fracture [17, 18], making the crushing behavior

*Corresponding author
Email addresses: elena.raponi@unicam.it (Elena Raponi), dario.fiumarella@polito.it (Dario Fiumarella), simonetta.boria@unicam.it (Simonetta Boria), alessandro.scattina@polito.it (Alessandro Scattina), giovanni.belingardi@polito.it (Giovanni Belingardi)

less controllable and predictable compared to the plastic collapse mode. In this context, the development of Computer-Aided Engineering (CAE) methods and the advances in numerical simulations using Finite Element Analysis (FEA) can enable prediction of component response to external loading conditions in the design phase of new products. Among others, the advanced multiphysics simulation software package LS-DYNA allows the modeling of a wide range of physical events thanks to a highly nonlinear transient dynamic FEA with explicit time integration. The material models available in the LS-DYNA software allow the simulation and prediction of the mechanical properties of composite materials starting from parameters that can be extrapolated by standard experimental tests. However, when these parameters are scaled up to simulate an entire component, the accuracy of the prediction decreases. To capture certain behaviors, such as collapse mode or crush energy at larger scales (e.g., component scale), more parameters are needed that typically cannot be defined by standard coupon tests. Moreover, polypropylene-based matrix composites show progressive crushing mainly caused by delamination and plastic deformation [19, 20], and these particular failure modes still make the finite element simulation of this class of materials an open issue [21, 22]. Therefore, many tests are usually necessary before a numerical model is obtained that agrees with the results from experimental tests.

An alternative to the direct numerical approach is numerical optimization [23–27]. For example, geometry optimization can be used to control the global crush behavior of a Carbon Fiber Reinforced Plastic (CFRP) component by triggering certain failure modes and thus avoiding catastrophic collapse [25, 28]. In this context, LS-OPT [29] is a numerical optimization tool that uses the LS-DYNA code to solve arbitrary nonlinear optimization problems and allows the user to structure the design process, explore the design space, and compute optimal designs based on given objectives and constraints. LS-OPT can be used to identify the material parameters associated with the use of advanced materials such as FRTP composites, which in particular require the application of highly complex material models. After performing the physical tests and setting a parameterized simulation of such tests with LS-DYNA, the optimizer allows an automated calibration of the numerical model to predict the test results. The aim is to minimize the error between the experimental results and the simulation results.

In this work, the optimization is applied to a Formula SAE impact attenuator made of an All-PP thermoplastic composite material [20] subjected to an axial impact load. The load-displacement curves extrapolated from the experimental tests are used here to calibrate the parameters of the numerical model by minimizing the Mean Square Error (MSE) between the experimental and numerical curves. Sequential optimization techniques based on surrogate modeling techniques are used for this purpose. Indeed, according to previous studies [30, 31], surrogate models (or meta-models) seem to be a valuable tool in structural optimization in the field of crashworthiness. Structural optimization is characterized by strong numerical noise, discontinuities in the objective function to be optimized, and physical bifurcations in the crash behavior, which make gradient-based optimization algorithms unsuitable. Based on a certain number of FEAs, surrogate models allow the construction of a computationally favorable approximation of the considered expensive objective function [32], also called response surface. In this way, direct optimization of the real objective function – which is very expensive, since it relies on FEA simulations – is replaced by optimization of the approximate model.

The aim of this study is to increase the accuracy of the prediction of the global crush behavior of the impact attenuator during the experimental crush test by using two different optimization approaches: the Successive Response Surface Method (SRSM) [33] and the Efficient Global Optimization (EGO) algorithm [34]. Both methods sequentially add points in the design space, i.e., in the domain of definition of the considered parameters, and are effective algorithms for highly nonlinear problems such as crashworthiness. However, while the former is characterized by a local search , the latter is more suitable for global optimization. Indeed, at each iteration, SRSM adds the same number of sampling points in an adaptive subregion and the optimization of the metamodel is restricted to the current subregion. On the other hand, EGO builds an initial response surface based on points added according to a Design of Experiments (DoE) technique [32], and continues by adding a single point per iteration according to the optimization of a low-cost function, the *acquisition function*, which balances local and global search. These algorithms are applied in this study with a particular focus on predicting the first part of the load-displacement plot. Indeed, previous studies have shown a dramatic discrepancy between the experimental and numerical curves during the initial impact phases. This was mainly due to initial contact instabilities between the impacting rigid wall and the component in the numerical simulations, as well as edge imperfections and undulations of the real component.

The potential of the presented methodology in the design of numerical simulations is confirmed by the obtained results, which allow several considerations. First, not all parameters have the same influence on the outcome of the

simulations and it is more convenient to select only some of them through a sensitivity analysis in order to save computational resources and obtain accurate results. Secondly, a focused study of the influence of the trigger – and thus the first stages of the crush – can lead to a more accurate prediction of the crush behavior. Finally, optimization by surrogate models is very effective in terms of computational cost. Although both considered optimization algorithms are capable of achieving comparable optimal configurations of parameters, the EGO algorithm requires a much smaller budget of evaluations – and thus FEA simulations – to achieve such optima. Moreover, it should be emphasised that thermoplastic composites are still the subject of intensive analysis studies due to their relative novelty. Thus, the result of this work represents an important step in the numerical characterization of the studied material, from which future research can also benefit.

The paper is organized as follows. Section 2 introduces the material PURE© used to fabricate the impact attenuator that is the focus of this study. In Sections 3 and 4, the mechanical [20, 35, 36] and numerical tests [37] previously performed on the component in question are each briefly recalled. In Section 5, an overview of the test cases considered for the optimization, the settings of the sensitivity analysis performed to estimate the influence of the different parameters, a brief theoretical definition of the optimization strategies SRSM and EGO, and a practical subsection on how to set up the solver LS-OPT for the analyses are given. The results are presented in Section 6 and the final conclusions are drawn at the end in Section 7.

2. Material

An impact attenuator of a Formula SAE Vehicle (Figure 1) made of an innovative thermoplastic composite material is considered for the analysis. The material is called PURE©, and both its matrix and reinforcement are made of polypropylene. The PURE© is a laminated composite and each lamina has a woven structure. The thermoplastic tapes present a skin and core configuration, that are respectively the copolymer and the homopolymer. Polymers generally present high degree of anisotropy, and orienting the polymer chain provides higher mechanical performances. Accordingly, the core of the tape is highly oriented towards providing strength. The tapes are manufactured with a co-extrusion process in which thin copolymer layers, which have lower melting temperature, cover directly the homopolymer. The tapes are woven into fabrics that are then hot-compacted in sheets. During this process the copolymer melts and, after solidification, it has bonding capability to keep the homopolymer fibers together. Hence, the copolymer form the matrix and the homopolymer the reinforcement of the final composite material. The advantage of this process is in the wide consolidation temperature window (130-180 °C) that ensure to keep high mechanical properties in the co-extruded tapes. Other advantages of the PURE© is the fully recyclability together with its manufacturing scraps, and its peculiar crush behavior. Indeed, the material has a good impact resistance, showing a soft and plastic impact behavior. The impact attenuator considered is a component intended to absorb energy and attenuate the impact acceleration during crash event. It has a truncated-cone geometry, where the frontal part has a lower cross-section, while the part fixed to the chassis has a wider cross-section. The thickness is variable along the axis of the attenuator (Figure 1): the red, green, and yellow portions have a thickness of 1.68 mm, 2.16 mm, and 2.4 mm, respectively. The variation of the thickness along the axis is designed to guarantee a progressive energy absorption during the collapse

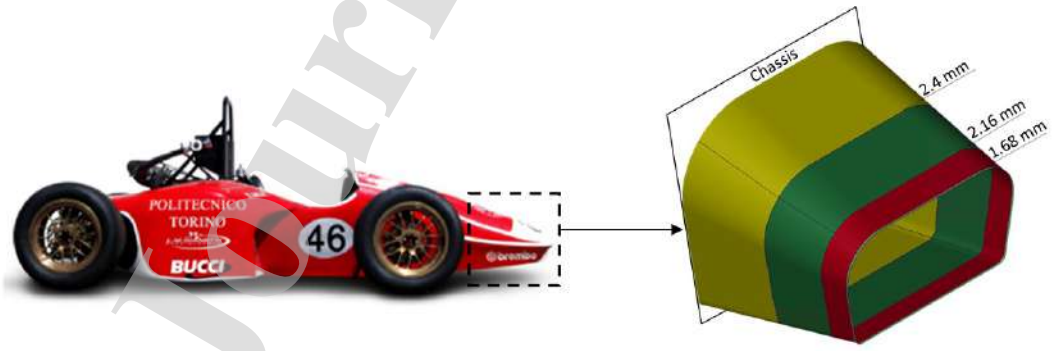

Figure 1: Formula SAE vehicle and zoom in on impact attenuator.

of the component. Although its relatively simple geometry, this component was chosen for the study according to its wide range of applications, that is not only restricted to the automotive sector, and that can be found in the aerospace industry too.

3. Experimental tests

Experimental tests were performed by the authors in previous works [20, 35, 38, 39], where standard coupon test were conducted to characterize the mechanical response of the material, summarized in Table 1.

Table 1: Experimental test results on standard PURE© specimens. E: Young Modulus; σ_u: strength; ε_u: maximum strain; G: shear modulus; τ_u: shear strength.

Test	E (GPa)	σ_u (MPa)	ε_u%
Tensile	3.4	217.8	5.90
Compression	5.1	17.5	0.52
	G (GPa)	τ_u(MPa)	ε_u%
Shear	11.15	21.64	0.065

From the tests, it emerged that the tensile behavior of the material is characterized by high elongation to failure and the failure is dominated by delamination. Failure due to delamination was confirmed also in compression tests, where the layers slipped causing a sort of packaging of the tapes. Both compressive strength and strain to elongation resulted largely lower than the tensile ones. The compression test on circular tubes showed a soft crush behavior. Indeed, the material failed in a ductile manner, following a non-regular folding of the layers. This plastic-buckling failure mode is due to the peculiar behavior of the thermoplastic polymer. No brittle failure happened, as is instead usually observed in common FRTS composites, where the catastrophic failure mode is mainly dominated by fiber rupture, matrix cracking, fiber-matrix debonding, and delamination [40]. Crushing tests on the PURE© impact attenuator confirmed that plastic mode is the dominant failure mechanism, as can be seen in Figure 2. Specifically, Figure 2a shows the set-up of the quasi-static crushing test on the impact attenuator. The load was applied along the axis of the attenuator by means of a moving metal plate that gets in contact with the upper section of the attenuator. The edge of this section presents imperfections and undulations, due to the cutting process that caused some fibers to debond. The results of the quasi-static test are shown in Figure 2b. The failure mode of the attenuator is mainly dominated by plastic deformation: the edge folded while crushing and the faces bent inward. No catastrophic failure occurred, as usually happen in common FRTS composites: the material did not splinter and no debrits formation occurred, leading to a more controllable and predictable crushing behavior. The load-displacement trend in Figure 3a shows four well distinguished peaks that are due to the thickness discontinuity along the component longitudinal axis. The curve evidenced a force that progressively and quite smoothly increases, and no sharp drop/peak of force are evident.

(a) (b)

Figure 2: Crush test set- up (a); Impact attenuator after crushing test (b).

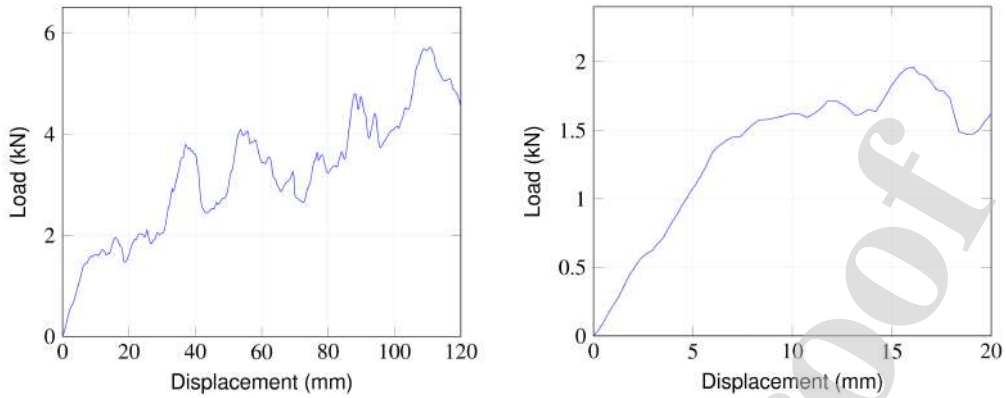

(a) (b)

Figure 3: Load-displacement experimental curves. (a) Curve recorded on the full range of displacement [0, 120] mm. (b) Zoom in on the first [0, 20] mm.

4. Numerical modeling

The finite element model of the component was built using the commercial software LS-DYNA PrePost version 4.8. The component was modelled with fully integrated four node shell elements of 2.5 mm of size. A PART COMPOSITE was defined to set the thickness of each integration point, the correct ply staking sequence, and orientation. The moving plate was modelled with a rigid wall. An automatic penalty-based contact definition (AUTOMATIC SINGLE SURFACE) ensured self contacts between the rigid wall and between the elements themselves. The rigid wall friction coefficient was estimated to lay between 0.2 and 0.3. A trigger, modelled as two rows of shell elements with two integration points along the thickness (Figure 4, grey elements), was added to the section of the impact attenuator that impacts with the rigid wall. The trigger aims to simulate the degraded properties of this edge, due to undulations and manufacture imperfections. In addition, the initial behavior of the crushing is highly influenced by the simultaneous contact of the elements of the upper section with the rigid wall, causing apparent force peaks during the early stages of the simulation. Consequently, two layers of elements with suitably degraded mechanical properties represent a mathematical expedient for solving this issue.

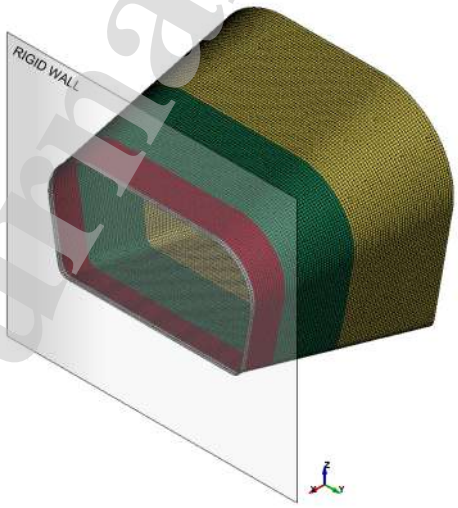

Figure 4: Numerical model of the impact attenuator.

The material card MAT 54/55 was used to model the thermoplastic composite, although the literature provides several examples where this material card is used to simulate FRTS composites [18, 28, 41]. This material card requires physical parameters of the material that are readily available through experimental tests, and some non-physical parameters that can be calibrated through optimization algorithms. The failure law chosen was the Chang Chang criterion [42]. Accordingly, the material card allows to set properties for the orthotropic direction of the material. The maximum element stress can be defined for element tension (Xt) and compression (Xc) in longitudinal direction and for element tension (Yt) and compression (Yc) in transverse direction. The characteristic loading curve of the element presents an elasto-plastic stress-strain relation. If strain to failure parameters are used (DFAIL parameters), the maximum deformation criteria is activated. The failure of the integration point, and consequently the element deletion is triggered by maximum strains in longitudinal and transverse compression and tension. In this material card, the crush front reduction factor (SOFT) is a fundamental parameter to be defined in crush simulations [41]. It is a non-physical parameter that reduces the strength of the element row ahead of the crush front, in order to reduce instabilities due to element deletion.

5. Optimization

The external optimizer LS-OPT was used to structure the design process, explore the design space and compute optimal parameter configurations, according to the specified objective. More in detail, two different analyses were performed: firstly, the material parameters that most influence the crash response were optimized; secondly, the influence of the trigger on the global response of the component was evaluated, and opportune geometrical and material card parameters influencing the physical and mechanical properties of the trigger were optimized. In the latter case, a sensitivity analysis was also performed with the aim to determine which variables have more impact on the output variability, hence to obtain a model simplification by fixing the parameters that are less relevant in view of the optimization target.

Differently from the methodology presented in [37], where the authors describe a targeted composite formulation of the optimization problem with load-history evaluations at specific displacements, here an ordinate-based curve matching optimization is performed. The Sequential Response Surface Method and the Efficient Global Optimization algorithm are implemented, whose details are provided in Section 5.3 and Section 5.4, respectively. In Figure 5, a flowchart of the proposed methodology is provided.

5.1. Test cases

Two surrogate-based optimization strategies are used to overcome the statistical uncertainties coming from experimental tests and the necessity to tune non-physical parameters. Moreover, in order to reach an accurate overlapping of the load-displacement curves resulting from the experimental tests and numerical simulations, two different test cases are considered, which are described in Section 5.1.1 and Section 5.1.2, respectively.

5.1.1. Material card optimization

The strain to failure calculated through experimental tests represents a loss of load-carrying capability of the PURE© standard specimen mainly due to delamination. However, this parameter does not scale up well to a larger component. Indeed, the crushing collapse of the PURE© impact attenuator is mainly dominated by creasing, folding, bending, and plastic deformation. Due to these discrepancies, a good match to the experimental data can be obtained using multiple combinations of MAT54/55 parameters. According to the literature [41] and to previous numerical analyses made from the authors, the compressive strain-to-failure in the fiber direction, DFAILc, is among the parameters that have the most influence on the crush response. Therefore, it is included in the optimization study. Moreover, in crashworthiness simulation, a crush front reduction factor called SOFT can be set. Its tuning can avoid instability and ensure stable crushing when the load goes from a row of elements to the following one. As such, it also strongly influences the crush simulation result, and is optimized as second and last variable of the optimization study. Therefore, a 2-dimensional optimization problem is addressed and targeted at minimizing the mean squared residual error, i.e., the difference in force values between the experimental and numerical load-displacement curves.

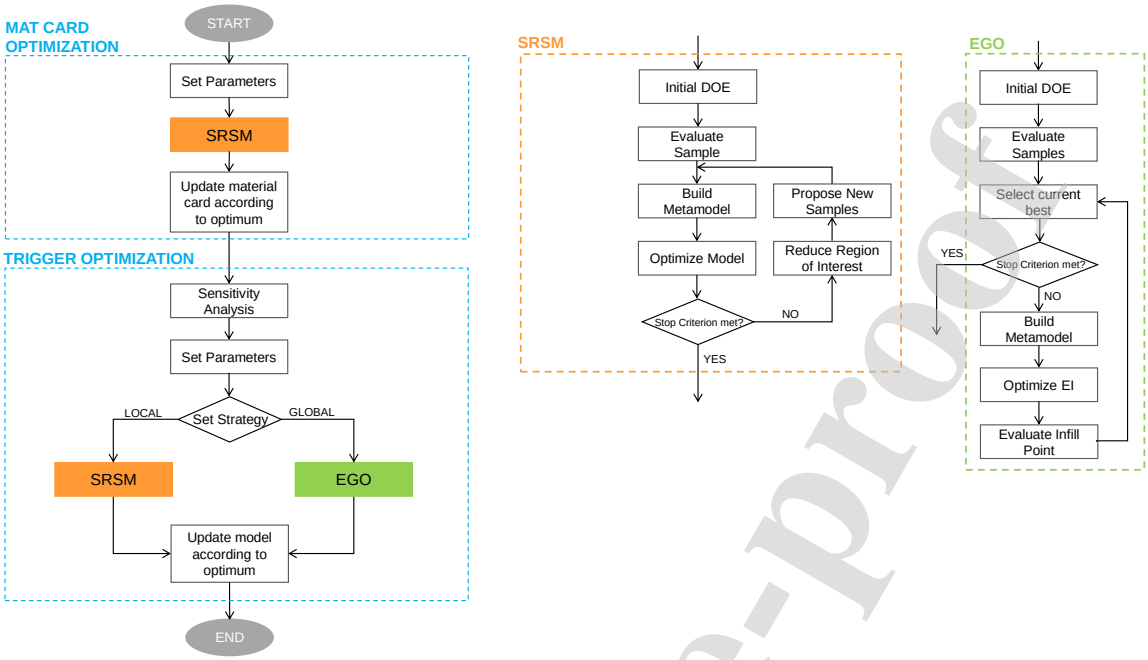

Figure 5: Optimization Methodology Flowchart. An enlargement of the steps composing the SRSM and EGO algorithms is provided on the right.

The optimization problems is defined as:

$$\begin{aligned} \min_{x_1, x_2} \quad & \text{MSE} = \frac{1}{P}\sum_{k=1}^{P}\left(\frac{f_k(x_1,x_2) - G_k}{M_k}\right)^2 \\ \text{s.t.} \quad & -0.35 \leq x_1 \leq -0.15, \\ & 0 \leq x_2 \leq 1, \end{aligned} \tag{1}$$

where x_1 and x_2 are the variables describing DFAILc and SOFT, respectively, and P is the amount of experimental force values acquired during the test. G_k , $k = 1, \ldots, P$, are the values on the experimental load-displacement target curve shown in Figure 3a, and $f_k(x_1, x_2)$ the corresponding components on the computed curve f resulting from a numerical simulation. M_k is defined as the maximum targeted absolute value of the experimental load-displacement curve, i.e., $M_k = \max|G_k|$. From the solver perspective, the displacement and force histories are extracted from the simulation output and afterwards used to construct a force vs. displacement crossplot. The experimental curves used as target curves are read into LS-OPT as file histories and the MSE between each crossplot and the corresponding test data is then computed.

5.1.2. Trigger optimization

According to previous numerical experiments simulating the impact on the component, there is always an early peak of force that is not visible in the experimental load-displacement curves. In order to reduce this discrepancy, an optimization study was carried out on the trigger parameters that directly affect the stiffness of the front part of the component. By calibrating them, it is possible to reduce the numerical instabilities and dampen the early force peak. These parameters are the Young Modulus (E_t), the compressive strain to failure ($DFAILc_t$), the maximum compressive strength (Xc_t), and the wall thickness (Tk). While the latter is a geometrical parameter, the former define the material card of the numerical model. The Tk variable indicates the thickness of a single integration point of the shell element composing the trigger part. The variation ranges of the four parameters can be observed in Equation (2), which defines the 4-dimensional optimization problem faced to obtain an accurate prediction of the part of the

load-displacement curve influenced by the trigger presence. The design ranges for the variables were determined according to the authors' experience and the initial design values associated with the numerical model, which were tuned by trial and error. The range should be neither too small, nor too large. Indeed, if the design range is small, there is a risk that it will be too conservative and may not allow the design to converge at all if it is too small to capture the variability of the response, especially if the objective function is characterized by noise. On the other hand, if the design range is too large, more samples are needed on the search space in order to achieve sufficient accuracy of the predictive model.

$$\begin{aligned} \min_{\boldsymbol{x}} \quad & \text{MSE} = \frac{1}{P}\sum_{k=1}^{P}\left(\frac{f_k(\boldsymbol{x}) - G_k}{M_k}\right)^2 \\ \text{s.t.} \quad & -0.35 \leq x_1 \leq -0.15, \\ & 1.5 \leq x_2 \leq 9.5, \\ & 0.01 \leq x_3 \leq 0.1, \\ & 0.01 \leq x_4 \leq 0.84 \end{aligned} \tag{2}$$

Here, the variables vector is $\boldsymbol{x} = (x_1, x_2, x_3, x_4)$, whose components represent in the order the parameters DFAILc_t, E_t, Xc_t, and Tk, while the other symbols are defined as in Equation (1). The subscript t in the variable names, which refers to the trigger component, is omitted and automatically implied in the following sections for simplicity and data readability. The experimental reference curve for the calculation of the MSE is shown in Figure 3b. It should be noted that, although kriging is a powerful surrogate model which results in high performance in terms of prediction quality, this method is costly in terms of computational complexity, especially for large datasets: the computational complexity of kriging is $O(n^3)$ where n is the number datapoints, i.e., measurements or simulations in our specific case. Moreover, the higher the dimensionality of the problem, the higher is the necessary number of datapoints in order to obtain an accurate approximation of the objective function. As such, a preliminary study on the sensitivity of the MSE objective function to the variability of the problem variables was carried out. This allowed for identifying the parameters that have more impact on the output variability and performing focused optimization studies taking into account a maximum of two variables in a single analysis.

5.2. Sensitivity Analysis

Since the design optimization process is expensive, suitable design parameters should be determined. At the beginning, it is important to select many rather than a few design variables. Afterward, it is commonly preferred to perform variable screening to reduce the number of design variables, and therefore the overall computational time. In this study, the Analysis of Variance (ANOVA) [43] is used to evaluate the main and interaction effects of the design variables defining the trigger on the computation of the MSE. ANOVA assesses the importance of one or more factors by comparing the response variable means, i.e. the averaged objective function values, at the different factor levels. A full factorial DoE sampling technique was here used to evaluate the objective function for every possible combination of every possible design variable [32]. This is the most straightforward way of sampling a design space, where each variable can assume only a prescribed number of discrete values, a.k.a. factor levels. In this study, three levels for each variable were chosen, leading to a total of $3^4 = 81$ DoE points. The levels for each factor are given in Table 2 and their combinations can be visualized in Figure 6, which provides an example of samples distribution involving the Tk, E, and Xc parameters.

Table 2: Factor information for the full factorial DoE generated in the sensitivity analysis study.

Factor	Levels	Values		
Tk	3	0.010	0.425	0.840
Xc	3	0.010	0.055	0.100
E	3	1.5	5.5	9.5
DFAILc	3	-0.40	-0.25	-0.10

Main effects plots and interaction plots were also evaluated. The former are used to examine the differences between level means for the single factors, while the latter show how the relationship between one categorical factor and a continuous response depends on the value of a second categorical factor, respectively.

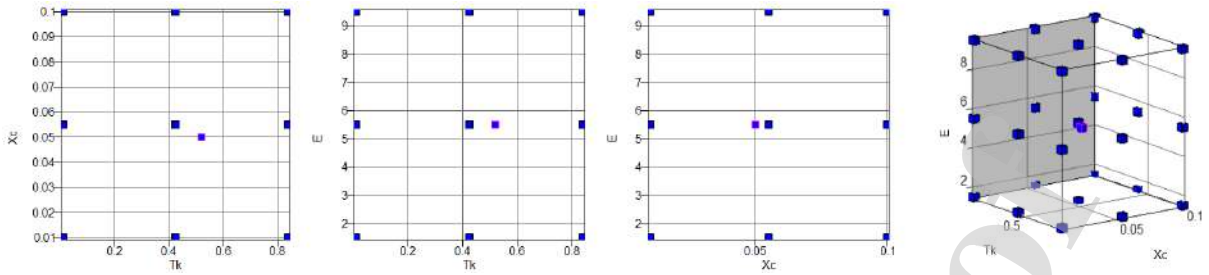

Figure 6: Example of Full Factorial sampling for a selection of parameters – Tk, E, and Xc – in 2D and 3D views. The highlighted sample refers to the initial configuration of parameters.

5.3. Sequential Response Surface Method (SRSM)

In the branch of metamodel-based optimization, which is used to create and optimize an approximate model of the design instead of optimizing the design through direct simulation, the first technique adopted in this study is the Sequential Response Surface Method (SRSM) [33]. The SRSM uses a region of interest – a subspace of the design space – to determine an approximate optimum. Sampling is done sequentially, meaning that only a small number of points is chosen for each iteration and multiple iterations are performed. After each iteration, a response surface approximating the real objective function is constructed over the parameters domain, it is optimized, and the domain is reduced to a new region of interest, centered on the current optimum. The algorithm proceeds by moving the center of the region of interest as well as reducing its size. The variables ranges for the next iteration depend on both the oscillatory nature of the solution and the accuracy of the current optimum. The first is based on whether the current optimum and the previous designs are on the opposite or the same side of the region of interest. Regarding this, it is worth noting that at the first iteration, the previous design is defined according to a configuration of parameters given as an input before the optimization is launched - the parameter configuration defining the baseline model in our case, i.e., the numerical model obtained with the trial and error technique. The accuracy of the current optimum is instead estimated using the proximity of the predicted optimum of the current iteration to the previous design. The smaller the distance between the two designs, the more rapidly the region of interest is reduced in size. In the current study, at each iteration a space filling sampling strategy is used to distribute points over the domain and the kriging metamodel is chosen to construct the response surface [32].

5.4. Efficient Global Optimization (EGO)

Efficient global optimization (EGO) [34] is a Gaussian process model-based adaptive algorithm finalized to reach a near-optimal solution by using a low budget of evaluations. The EGO algorithm begins by fitting a surrogate model to a set of initial points specified according to a DoE scheme. Even in this case, the DoE sampling scheme is the space filling design and the response surface is constructed according to the kriging surrogate model. While the DoE scheme is arbitrary, the choice of the surrogate model is strictly dictated by the optimization strategy. Indeed, after the first response surface is fitted according to the training points – DoE points and related objective function evaluations – for all iterations a new point, referred to as *infill point*, is selected by maximizing an Expected Improvement (EI) function [32], which is defined as follows:

$$E[I(\boldsymbol{x})] = \begin{cases} (y_{min} - \hat{y}(\boldsymbol{x}))\Phi\left(\frac{y_{min}-\hat{y}(\boldsymbol{x})}{\hat{s}(\boldsymbol{x})}\right) + \hat{s}(\boldsymbol{x})\phi\left(\frac{y_{min}-\hat{y}(\boldsymbol{x})}{\hat{s}(\boldsymbol{x})}\right) & \text{if } \hat{s}(\boldsymbol{x}) > 0, \\ 0 & \text{if } \hat{s}(\boldsymbol{x}) = 0. \end{cases} \tag{3}$$

In Equation (3), $\hat{y}$ is the function approximating the real and expensive objective function, y_{min} is the best objective function value observed in all the previous iterations, $\hat{s}$ represents the uncertainty on the interpolated function value, while Φ and ϕ are the Gaussian cumulative distribution function and probability density function, respectively. Therefore, the EI not only considers the predicted response value, but also its variance. The error committed in the approximation $\hat{s}$ is utilized to balance between local and global search. In fact, Equation (3) allows for locating new points in promising areas, close to locations where the best fitness function value has been computed, as well as in sparsely sampled areas, which are characterized by a low sampling density and, consequently, high uncertainties.

Indeed, according to Equation (3), the EI can be large due to any of the two additive terms — the first governed by the prediction mean and the other by the prediction variance. The point with the maximum EI is evaluated to update the Kriging model, i.e., a FEM simulation is performed and the objective function value associated to the output is compared to one of the best sample so far and used to augment the training set on which the response surface is fit. The infill procedure is repeated until a prescribed number of evaluations is reached.

5.5. Setup in LS-OPT

The software LS-OPT was used to carry out the optimization of (1) the material card parameters SOFT and DFAILc based on the match between the entire load-displacement curves from experimental tests (Figure 3a) and simulations, and (2) the most influencing parameters on the trigger behavior, and hence the first portion of the load-displacement curve depicted in Figure 3b, identified thanks to the ANOVA test. The focus of this section is to describe the optimization from the software perspective, by providing a visual depiction of the methods flow and useful details about the options settings to run the algorithms. Since the trigger optimization was addressed through both SRSM and EGO, this test case is here used to illustrate the logical flows and the technical details.

Figure 7 illustrates the LS-OPT graphical user interface, where the optimization flowchart of the SRSM is displayed. Once the parameters undergoing the optimization procedure are defined, the flow starts with the sampling phase, where a Design of Experiments methodology [32] is used to sample the design space. In particular, a Space Filling sampling strategy is chosen to locate a set of evenly distributed points over the prescribed domain so that the minimum distance between any two points is maximized. The objective function is evaluated by performing FEM simulations on models defined according to the parameter configurations associated to each DoE point. The load-displacement curves are derived from the simulations, and the MSE is computed for each curve and assigned as objective function value to the single sampling data point. In this way, it is possible to describe the variation of the objective function based on the values of the design variables affecting the process. Once the training set is available, the whole domain is defined as Region of Interest and a response surface through the Kriging metamodel [32] is built upon the available datapoints. In our case, exponential correlation functions and a quadratic trend model are chosen to define the level of regression of the model and the polynomial degree of the approximation, as was done in [37]. The optimum of the objective function is determined on the approximated response surface by using a Genetic Algorithm [44], with the default settings provided by LS-OPT. The optimum is evaluated and is taken as the first sample of the following iteration, where a new region of interest is defined as a portion of the one of the previous iteration, and the center is located on the previous optimum. On the restricted domain, the described steps – sampling, approximation construction, optimization – are repeated until a given termination criterion is met, which in our analyses is fixed to a total number of 5 iterations. By setting 10 evaluations per iteration, this termination criteria implies a total budget of 50 evaluated sample points. In the last iteration, the sample points are located in a region of interest that is small enough to consider a satisfactorily small range of variability in the data. The optimization terminates with a verification simulation on the computed optimum.

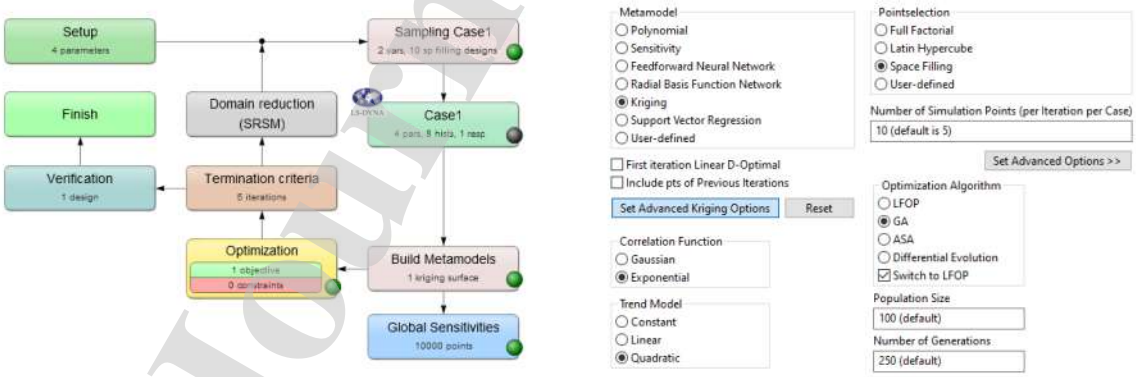

Figure 7: Optimization flowchart in LS-OPT for the SRSM optimization strategy. The main settings are shown on the right.

The LS-OPT interface for the EGO algorithm is illustrated in Figure 8. EGO is a separate metamodel-base optimization strategy in LS-OPT, which restricts the choice of the metamodel to kriging, since it is able to take advantage of its ability to estimate the potential error committed in the approximation. Indeed, the maximization of the EI function defined in Equation (3) allows for locating points in the domain area containing the current best design, as well as in scarcely sampled regions, characterized by an high variance of the model. The optimization happens in two steps. The first step (Step 1) consists of a unique iteration, set as shown in Figure 8, on the left. First of all, a DoE

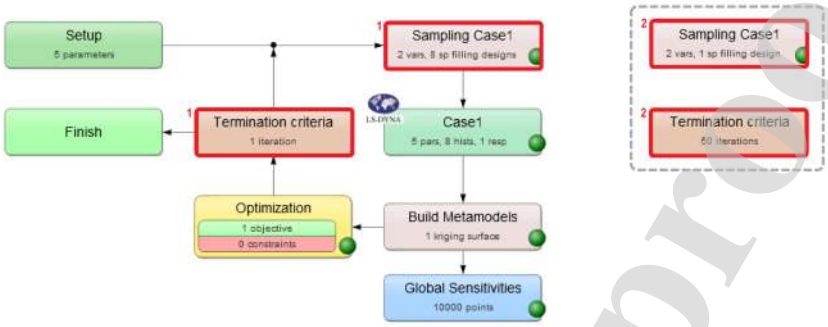

Figure 8: Optimization flowchart in LS-OPT for the EGO optimization strategy. The red frames highlight the diagram blocks that differ for the two steps – Step 1 and Step 2 – of the optimization process.

of multiple points is performed. Again, a Space Filling design was chosen to locate 8 sample points. Based on that, the kriging response surface is built and an approximated value of the objective function $\hat{y}$ as well as the error committed in the approximation $\hat{s}$ are associated to each point of the search domain. Hence, the EI function is built over the same domain, and its optimization returns the infill point to be evaluated through FEM simulation. Step 1 is followed by a sequential EGO with one sample per iteration (Step 2), as shown by Figure 8 (right). The switch from Step 1 to Step 2 is practically handled by letting the first iteration end and changing the algorithm settings before restarting the optimization run from the second iteration. In the sequential EGO, one infill point per iteration is added, and the response surface is updated at each iteration based on all the previous points (i.e., DoE samples and infill points). It is worth noting that, at the end of every iteration, the current best design is updated if the simulated infill point has a better objective function value than the best so far, that is the best among the DoE points and all the previous infill points. Even in this case, the algorithm stops when a prescribed number of 50 iterations is reached, which is a reasonable budget for the addressed 2-dimensional optimization problem [31] and in line with the total budget used for the SRSM optimization strategy. Alternative termination criteria are design change or objective function tolerances.

6. Results and discussion

The load-displacement curve of the experimental crush test on the impact attenuator is shown in Figure 3a. Four peaks of force can be distinguished in the curve. These peaks are due to thickness discontinuity, as illustrated in Figure 4, and layer compaction. The material did not splitter: the faces folded and compacted themselves. The curve evidenced a force that progressively and quite smoothly increases, an no sharp drop/peak of force are evident.

The numerical material model was set-up according to the outcome of the standard experimental tests: the Young modulus, the ultimate strain and the stress in tension and compression were computed experimentally and then used as input parameters. However, these parameters are affected by statistical uncertainties, and the SOFT non-physical factor cannot even be experimentally evaluated. Accordingly, a trial and error process was necessary to fine-tune the material parameters, and through this process, a high sensitivity of the response to the variation of the SOFT and DFAILc parameters was evident. Figure 9a shows a comparison of the collapse mode between the experimental and the simulated component, calibrated by trial and error. The faces of the experimental attenuator undergo to buckling and layer compaction (Figure 9a). Instead, the faces of the numerical model do not compact due to element failure and deletion (Figure 9b-9c).

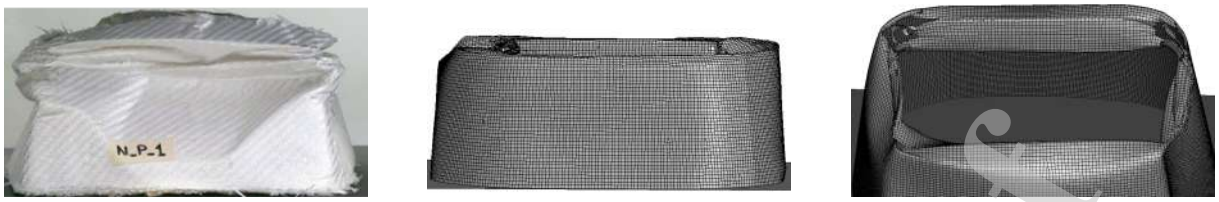

(a) (b) (c)

Figure 9: Crush behavior: (a) experimental test and (b)-(c) numerical simulation.

6.1. Material card optimization

The DFAILc and SOFT parameters of the material map were optimized using the SRSM methodology described in Section 5.3. A total budget of 4 iterations, each with 8 simulated sample points, was considered. This choice is motivated by a trade-off between computational cost and accuracy. After the fourth iteration, the algorithm chooses a sufficiently reduced range that allows to consider a satisfactorily small range of variability in the data. The sample points are arranged according to a space-filling DoE scheme that allows points to be generated by maximizing their mutual distances. The MSE kriging response surface is then adjusted based only on the sample points of the current iteration to obtain a locally accurate approximation and easily drive the search for the optimum towards the restricted region of interest. As can be seen in Figure 10, the domain tends to shrink around the predicted optimum by focusing the search on lower DFAILc values.

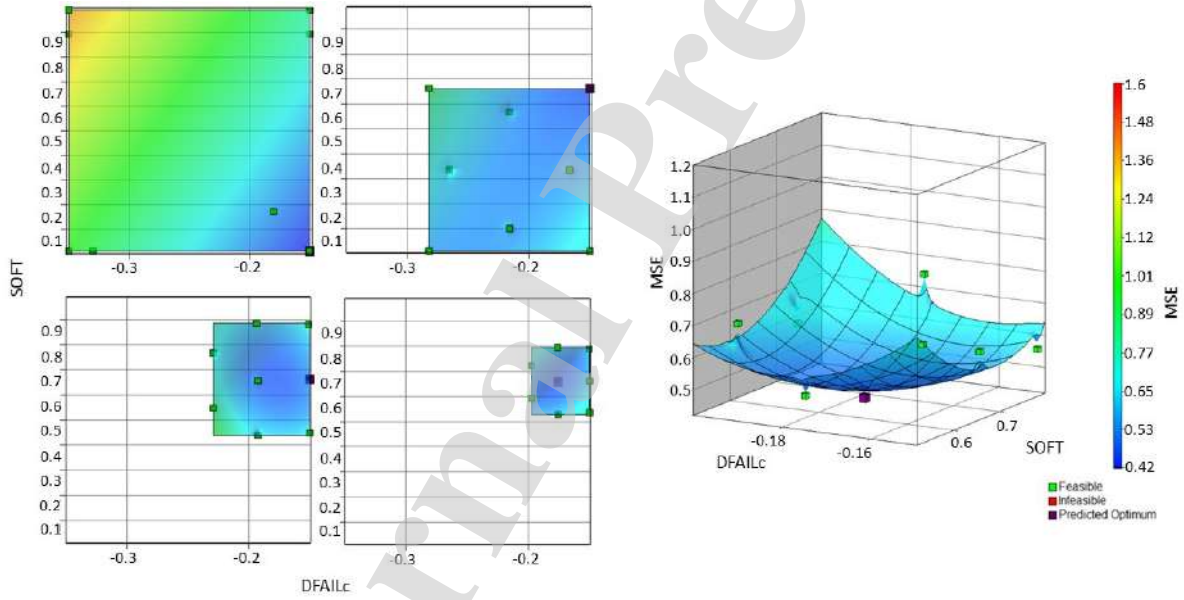

Figure 10: Top views of the metamodel approximations for the 4 iterations of the SRSM optimization procedure for the material card optimization. The response surface of the last iteration is also shown in isometric view.

Starting from the search domain D = $[-0.35, -0.15] \times [0.01, 0.99]$, it ends up to the optimum (DFAILc, SOFT) = $(-0.17, 0.66)$, which corresponds to an MSE amounting to 0.440. However, low DFAILc values lead the elements to fail and erode at low deformations, resulting in an overall brittle-like behavior and decreasing the average load. Figure 11 shows the optimal result of the optimization. It can be appreciated how the global behavior follows that of the experimental curve. The peak around 40 mm, corresponding to the first thickness increase, is well captured. A substantial difference can be noticed around 55 mm. In fact, experimentally, this peak of force is due to the compaction of the bent layers of the attenuator's edges. The numerical simulation, on the other hand, does not exhibit

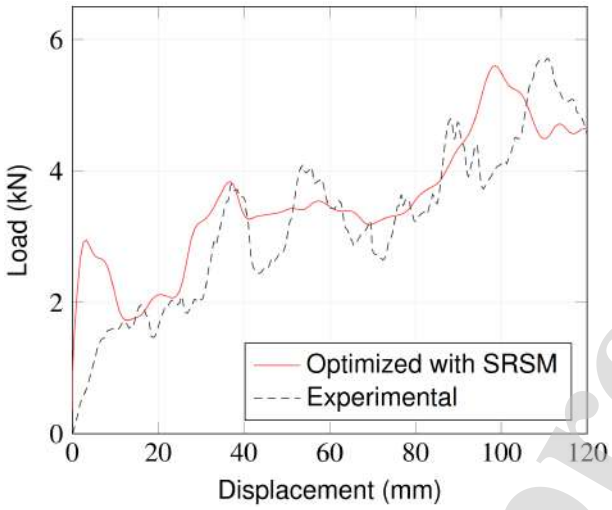

Figure 11: Comparison of the experimental load-displacement curve with the optimized numerical curve obtained by SRSM Methodology

this compaction behavior, as the elements tend to fail before the lateral faces of the attenuator compact themselves (Figure 9c). Finally, it is possible to appreciate a marked discrepancy of the initial peak between the simulated curve and the experimental curve. This discrepancy is evident both in terms of peak force (difference of around 50%) and in terms of stiffness, and was attenuated by implementing and optimizing a numerical trigger, as described in the following sections.

6.2. Sensitivity analysis on the trigger parameters

As introduced in Section 5.1.2, the influence of 4 variables (Tk, Xc, E, DFAILc) on the trigger response was analyzed in order to find the factors that most influence the crush response on the first displacements. Each point of the DoE corresponds to a crush simulation on the first 20 mm of the component, according to each combination of the 4 factors, as described in Section 5.2. In fact, the influence of the trigger on the force response is evident within the first moments of crushing. Furthermore, this choice allows to considerably reduce the computational time of the simulations. Figure 12 shows the main effects plot for the MSE between the numerical and the experimental curve. This plot evaluates the differences between the fitted means of the levels for each factor analyzed. Each point represents the response mean of the factor. If the responses of a factor are placed horizontally, then it can be stated that the factor has not a strong influence on the response.

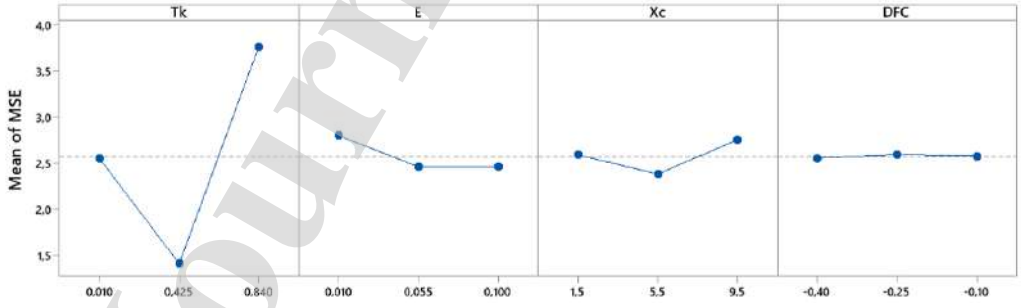

Figure 12: Main Effects Plot evaluated on the MSE response, with data averaged on each factor level.

From this graph it is evident that the DFAILc value has no influence on the evaluated response. Instead, the thickness seems to have a strong effect on the MSE value. However, it is of great importance to evaluate the relationship

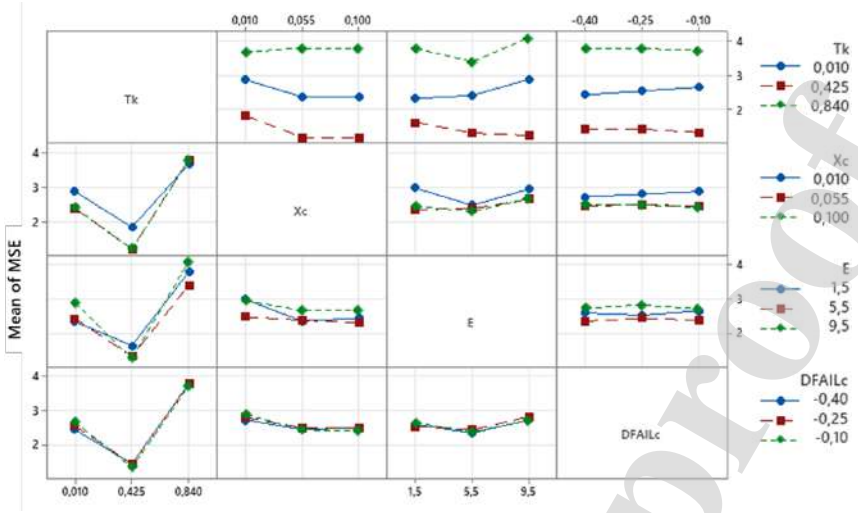

Figure 13: Interaction Plots for MSE, with data averaged on each factor level.

Table 3: Factor information for the full factorial DoE generated in the sensitivity analysis study.

Variable	P-Value
Tk	0
Xc	0
E	0
DFAILc	0.87
Tk*Xc	0
Tk*E	0
Tk*DFAILc	0.42
Xc*E	0.06
Xc*DFAILc	0.73
E*DFAILc	0.73

that the interaction between two factors has on the response value. Figure 13 shows the interaction plots, representing the means for the levels of one factor on the x-axis, and a separate line for each level of another factor. The interaction between DFAILc and the other three factors is confirmed to be inconsistent. The DFAILc vs Tk plot presents straight horizontal lines, meaning that a change in DFAILc does not affect the outcome. The three lines are parallel but quite distant from each other, confirming that the Tk value has a stronger effect. The DFAILc vs Xc and the DFAILc vs E plots present straight parallel lines too, even if they are closer each other, suggesting that these two parameters have a poor effect on the response. For completeness, Table 3 shows the results of the analysis of variance (ANOVA) carried out with a significance level of 5 percent. For the values of Tk, Xc, and E, it is not possible to accept the null hypothesis. Mixed terms of the second order were also analyzed. In this case, the interactions between Tk and Xc, and between Tk and E turn out to influence the response. Mixed terms of the third order were evaluated too, and was confirmed that the terms containing the DFAILC variable have not influence on the response. Consequently, the parameters Tk, Xc and E were used for trigger optimization, reducing the dimension of the problem to 3 variables.

It is clear from the interaction plots (figure 13) that the Tk variable has the stronger effect on the response. Figure 14 shows the effect of the only trigger thickness on the component stress distribution after the first 7 mm and 14 mm of crush displacement. It is evident how a reduced thickness leads the effect of the trigger being null. The load remains almost zero (Figure 15) for the first two millimeters of crushing. Afterwards, the elements of the upper edge of the component get in contact with the rigid wall at the same time, causing a sudden increase of the load. On the other

hand, a thick trigger causes a noticeable increase in load during the early stages of the impact. The elements of the trigger transfer the load directly to the underlying elements, before these come into contact with the rigid wall. As can be noticed in Figure 14, the elements above the top section are more loaded, and greater out of plane deformation and bending of the vertical faces are evident. An intermediate trigger thickness, would hence guarantee a softening effect on the upper edge of the nose. Indeed, it is possible to appreciate the triggering of some folds, from which the deformation propagates more regularly.

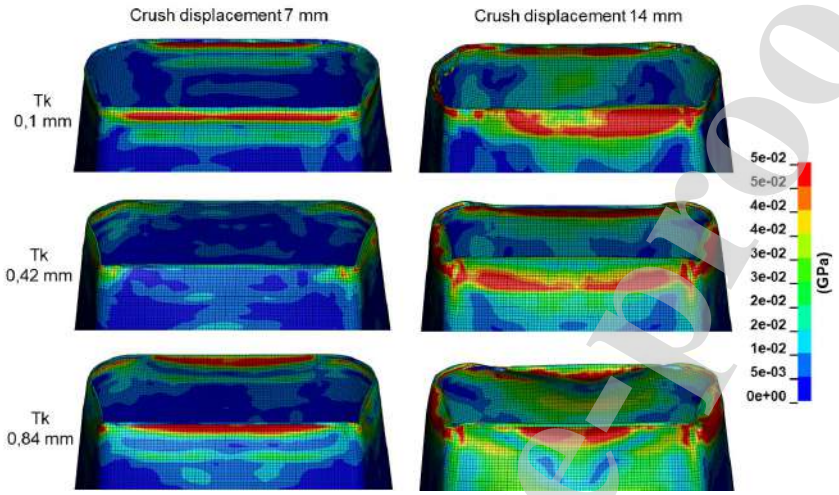

Figure 14: Stress distribution of the impact attenuator crush according to the thickness of the trigger.

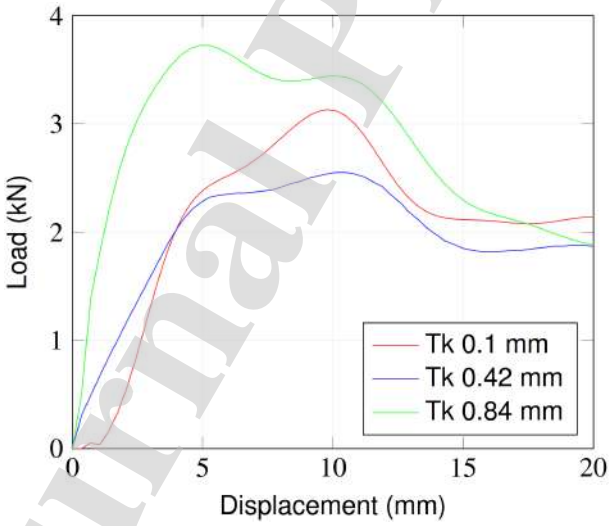

Figure 15: Influence of the trigger thickness on the force-displacement trend.

6.3. Trigger optimization

Based on the outcome of the sensitivity analysis, the trigger optimization was performed using both the SRSM and EGO optimization strategies, by focusing on the parameters that have the greatest impact on the variability of the objective function. Initial experiments with the SRSM have empirically shown that this optimization technique tends to over-localize the search. In contrast, the EGO algorithm has high potential because it constructs and optimizes an

acquisition function that balances exploitation (evaluating points with low mean) and exploration (evaluating points with high uncertainty) of the search domain. The error that the kriging surrogate model makes in approximating the real objective function is not used at all in the SRSM, since the optimum of the response surface is simply found by a genetic algorithm. EGO has been applied both to a one-dimensional optimization problem, where the thickness is the only variable, and to two-dimensional problems, where the thickness is optimized together with either the modulus E or the strength to failure Xc. All the parameters that do not undergo optimization are kept constant according to the outcome of the material card optimization on the full load-displacement curve described in Section 6.1.

6.3.1. SRSM on Tk and Xc

At first, the Tk and Xc parameters are estimated by using an SRSM iterative procedure. It is composed of five iterations, each of which starts from a DoE sample set of 10 points that are located on the domain according to a space-filling scheme, which allows for generating samples that are evenly distributed allover the current region of interest, as shown in Figure 16. From the figure, it is evident that at each iteration the region of interest is reduced and centered on the predicted optimum of the preceding iteration. The evolution of the region of interest is particularly

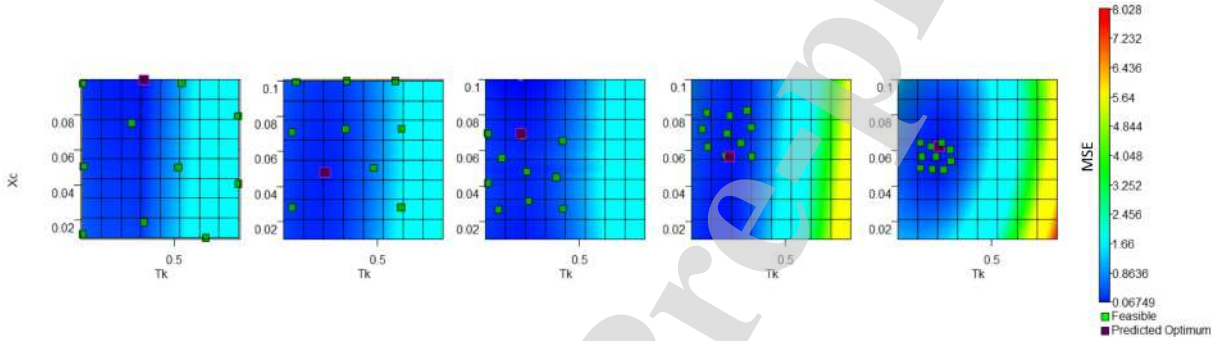

Figure 16: Top views of the metamodel approximations for the 5 iterations of the SRSM optimization procedure for the trigger optimization on the Xc and Tk variables.

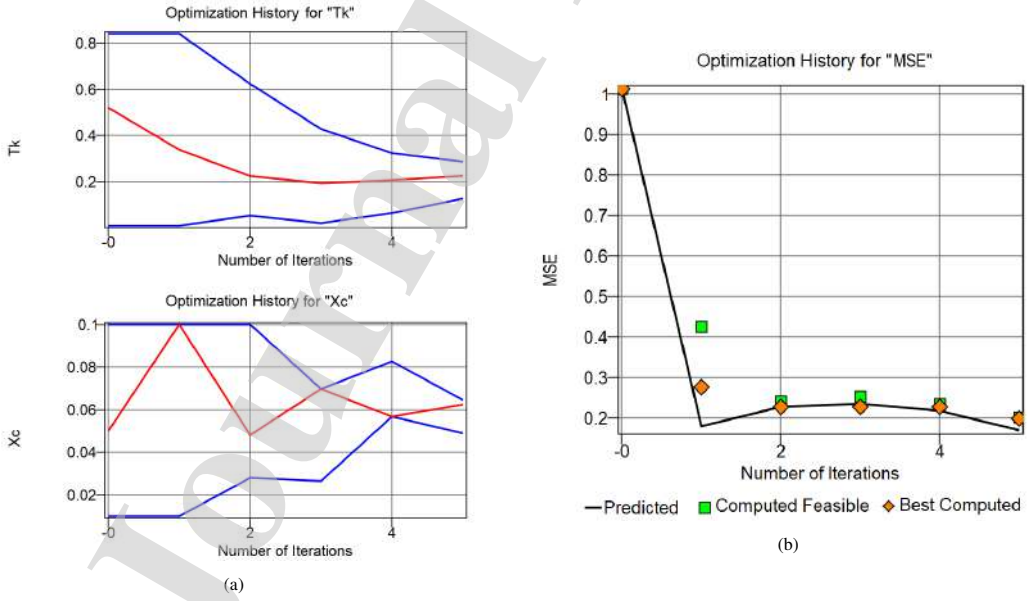

Figure 17: Histories of variables (a) and objective (b) for the SRSM optimization strategy over the 5 iterations.

appreciable in Figure 17a, where the history of the predicted optimum (red curve) and the range of the domain of variation (blue curves) are clearly shown. Starting from a parameters configuration equal to (Tk,Xc)= $(0.52, 0.05)$ for the baseline model, i.e., the one set through trial and error, the parameters configurations defining the predicted optima found in the five iterations are shown in Table 4. It should be noted that, while for the thickness parameter the

Table 4: Evolution of the significant samples for the SRSM applied to the optimization of Tk and Xc.

	Iteration 1		Iteration 2		Iteration 3		Iteration 4		Iteration 5	
	Point (Tk, Xc)	MSE	Point (Tk, Xc)	MSE	Point (Tk, Xc)	MSE	Point (Tk, Xc)	MSE	Point (Tk, Xc)	MSE
Predicted Optimum	(0.34, 1)	0.180	(0.22, 0.048)	0.227	(0.19, 0.070)	0.235	(0.21, 0.057)	0.218	(0.25,0.062)	0.170
Computed Optimum	(0.34, 1)	0.426	(0.22, 0.048)	0.227	(0.19, 0.070)	0.253	(0.21, 0.057)	0.234	(0.25,0.062)	0.201
Best Computed	(0.27, 0.045)	0.276	(0.22, 0.048)	0.227	(0.22, 0.048)	0.227	(0.19, 0.057)	0.227	(0.18, 0.062)	0.199

optimum is always internal to the variation range, the Xc variable often ends up being located on the boundaries of its definition domain. This can be interpreted as a too strong tendency of the algorithm of localizing the search, with the possibility of missing important information on the neglected domain areas.

The predicted optimum of each iteration is evaluated through numerical simulation and used as DoE point of the following one. In Figure 17b, the objective function value of this point is represented and referred to as *Computed Feasible*. In line with this, the term *Computed Optimum* is used to refer to the combination of parameters that is found at the end of the sequential optimization strategy as the point that optimizes the last MSE approximation model, while the *Best Computed* is the parameters configuration that shows the lowest MSE among all the points that have been evaluated during the optimization procedure. It can be observed that the Best Computed is not updated during the second, third, and forth iterations, and only the fifth iteration is able to furnish a prediction that also leads to a reduction of the MSE between the experimental and numerical curves. As illustrated in Table 4, the minimum MSE value is found with the parameters configuration (Tk,Xc) = $(0.25, 0.062)$, which provides an MSE of 0.199.

6.3.2. EGO on Tk

By observing both, the main effects plots in Figure 12 and the interaction plots in Figure 13, it is clear that the MSE objective function is mainly influenced by the trigger thickness. On the other hand, the maximum strain for fiber compression DFAILc is practically insignificant. As such, the good convergence properties of the EGO strategy were first tested on a one-dimensional problem with Tk as unique parameter, and on two-variables problems afterward. The former test case is described in this section.

Starting from a space-filling DoE of 4 points, Figure 18 shows the evolution of the kriging approximation over the 15 EGO iterations that were performed, with 1 infill point each. In the figure, the new sample chosen according to the maximization of the EI acquisition function is highlighted and, based on it, the model is refitted at each iteration. It can be noted that the new point is sometimes located by the algorithm in the most promising area of the domain, i.e., the region containing the current best design, while other times it moves away from the optimal area to explore sparsely populated regions. This attitude is also evident in Figure 19, which shows the optimization history of both the infill point and the best computed until each iteration. Indeed, when the MSE value of the computed feasible is much higher than the one of the best computed, it means that the EI maximization locates the infill point in a less populated region of the domain, where the approximation model might not be not accurate and, as a consequence, a new point located there would likely be far from optimality. Of course, the best computed is updated only if the new infill point has a better objective function value than the best so far, therefore its history decreases monotonously. From the optimization history, it is evident that the optimum predicted in the first iteration following the initial DoE procedure actually represents the best computed throughout the prescribed budget of iteration, that corresponds to the total budget of finite element simulations. Indeed, this optimization test case benefits from both, its low dimensionality and the exploitative/explorative capabilities of the EGO algorithm. However, it is worth underlining that reducing the search space to only one variable is equivalent to searching for the optimum within a subspace of the actual 4-dimensional domain defined by Equation 2, thus limiting the algorithm freedom during its search. Indeed, EGO converges to the optimal point with Tk = 0.21 mm and an MSE value of 0.249, which is worse than the best computed from the SRSM strategy on 2 parameters, but, since it was reached after only 5 objective function evaluations (i.e., FEM evaluations of the numerical model), can be considered satisfactory given the trade-off between prediction accuracy and saving of computational resources. We hence decided to use the same optimization strategy to optimize couples of parameters in order to exploit the interaction effects between them: Tk and E first, and Tk and Xc afterward.

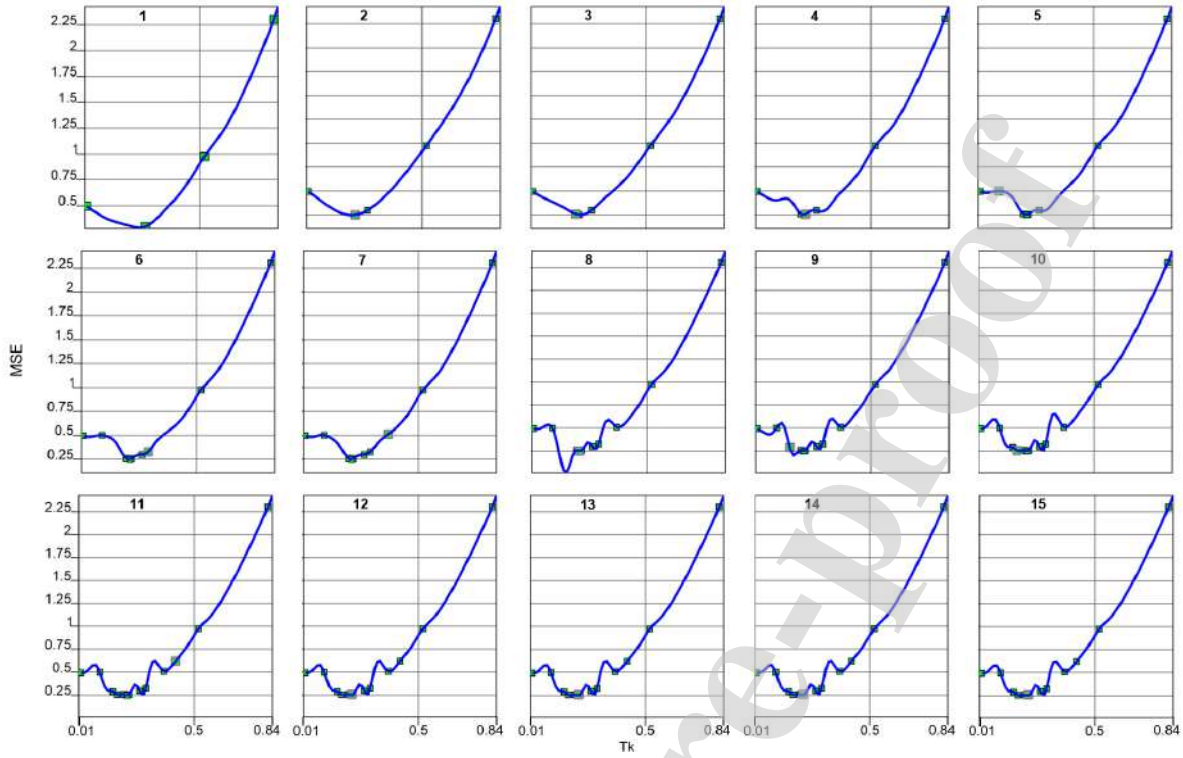

Figure 18: Evolution of the kriging model approximation of the MSE objective function for Tk $\in [0.01, 0.84]$, based on the initial 4 DoE points and the new infill point per iteration.

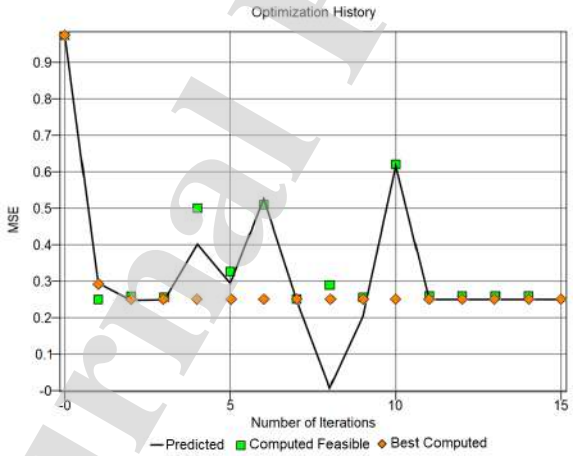

Figure 19: Optimization history of the EGO algorithm applied to the optimization of Tk by minimizing the MSE between experimental and numerical load-displacement curves. Both the histories of the infill point and the best computed are shown, together with the predicted optimal value of the EI function.

6.3.3. EGO on two parameters

The limitations showed by the optimization on the one-dimensional test case drove the investigation towards the usage of the EGO algorithm on the optimization of couples of parameters: (Tk, E) and (Tk, Xc). Both the optimization studies start from an 8-samples space-filling DoE scheme on a bi-dimensional search space defined for

each case according to the variables boundaries specified in Equation (2). At each iteration, a kriging response surface is fitted on the available training data, leading to a global prediction of the MSE objective function. Again, based on that and the available points, the EI acquisition function is built and optimized through genetic algorithm. The predicted optimum is evaluated, compared to the best computed so far withing the optimization procedure, and used to update the approximation model for the following iteration. If the simulation returns an objective function value that is better than the best so far, then the infill points becomes the best computed – y^* in Equation (3) – and the optimization proceeds with the following iteration. The optimization history of the predicted optimum, the computed optimum, and the best computed is shown in Figure 20a and Figure 20b for the (Tk, E) and the (Tk, Xc) test case, respectively. In both plots, the mixed exploitative/explorative attitude of the EGO algorithm can be observed thanks to

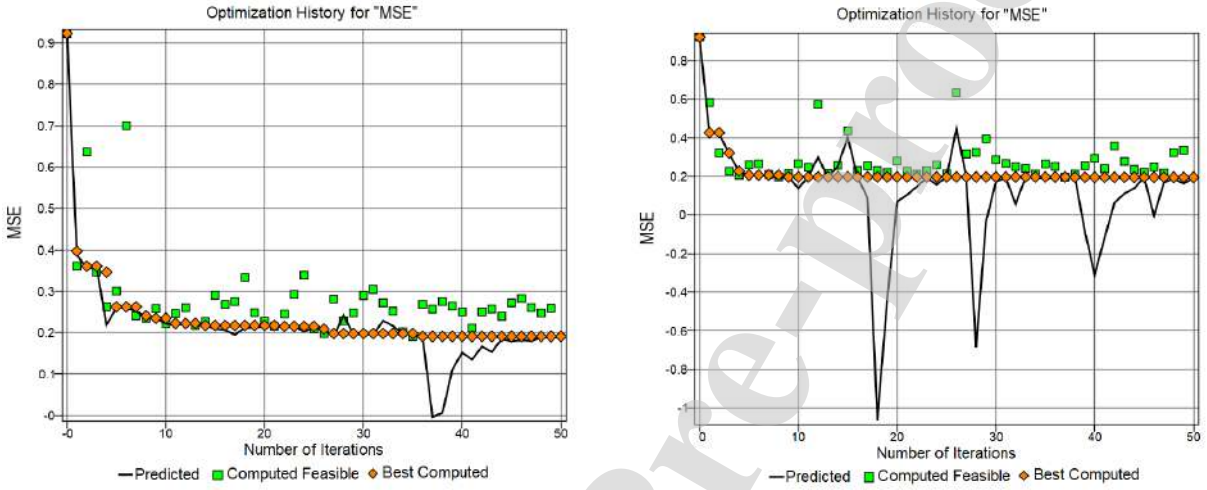

(a) (b)

Figure 20: Optimization history of the EGO algorithm applied to the optimization of (a) Tk and E and (b) Tk and Xc variables, by minimizing the MSE between experimental and numerical load-displacement curves.

the evident variation in the computed objective function values of the infill points, i.e., the predicted optima through the maximization of EI. In a total budget of 50 evaluations in addition to the ones needed for the DoE phase, the best computed undergoes several updates, leading to the final optimal samples (Tk, E) = $(0.22, 6.87)$ and (Tk, Xc) = $(0.18, 0.089)$. The respective objective function values are MSE$(0.22, 6.87)$ = 0.191 and MSE$(0.18, 0.089)$ = 0.197. Hence, both the bi-dimensional test cases allow for obtaining a lower MSE than the optimization of the thickness parameter by itself, which means that interaction effects are not totally negligible. On the other hand, by keeping in mind that in Section 6.3.2 the best computed is found by using 5 FEM simulations, EGO converges to an optimal values much faster and with much less computational effort when optimizing one variable only. All in all, it is worth underlining that both the values found for the Tk parameters are very close to the value found in the one-dimensional optimization problem (Tk = 0.21 mm).

6.3.4. Considerations on the optimization results

In order to assess the accuracy of the load-displacement numerical curves compared to the experimental one, three error measures have been evaluated: the Root Mean Squared Error (RMSE), the coefficient of determination (R^2), and the maximal residual error (ε_{max}). The computations are performed by interpolation of the experimental and numerical load-displacement data at 20 and 120 query points when interested on the [0, 20] mm and [0,120] mm displacement ranges, respectively. Good agreement is stated when the RMSE and the ε_{max} measures present a small value, whereas the R^2 should have a value close to the unit [29]. To draw some general conclusions, the optimal parameters configuration found in the trigger optimization test cases were used to run verification FEM simulations on the full displacement range of interest, [0, 120] mm. Indeed, the studies aimed at optimizing the most relevant parameters of the trigger component were set to maximize the coherence between experimental and

numerical curves in the range [0, 20] mm, which corresponds to the portion of curve that is most influenced by variation in the trigger set up. As a consequence, it is not obvious that parameters configurations minimizing the MSE on the first 20 mm are optimal for the full range of displacements too. Table 5 contains the aforementioned accuracy measures evaluated on the outcome of the final verification FEM simulations. The accuracy is evaluated for the optimal parameter configurations resulting from every performed study, except for the SRSM optimization on the trigger component. Indeed, it resulted to be a too exploitative search technique, and hence a priori less reliable than EGO for the case of interest. It can be observed that the numerical curve tuned by trial and error is less accurate

Table 5: Accuracy estimation of the numerical approximation of the full load-displacement curves from the experimental tests. Bold style highlights the best results.

	RMSE	R^2	ε_{max}
trial and error	0.78683	0.58768	2.5776
SRSM Full	0.70997	0.67118	2.1101
EGO Tk	0.66460	0.68574	**1.2761**
EGO Tk/E	**0.60536**	0.70444	1.5250
EGO Tk/Xc	0.65767	**0.71191**	1.3603

of any other curve according to each error measure, proving an improvement lead by surrogate-based optimization strategies. Moreover, when evaluated on the full range of displacements, the optimal solutions from the optimization studies on the trigger component perform better than the optimum of the SRSM result obtained by minimization of the MSE computed on the full load-displacement curve. This means that a focused study on the trigger component is beneficial for improving the overall accuracy of the numerical load-displacement curve. This can be also observed

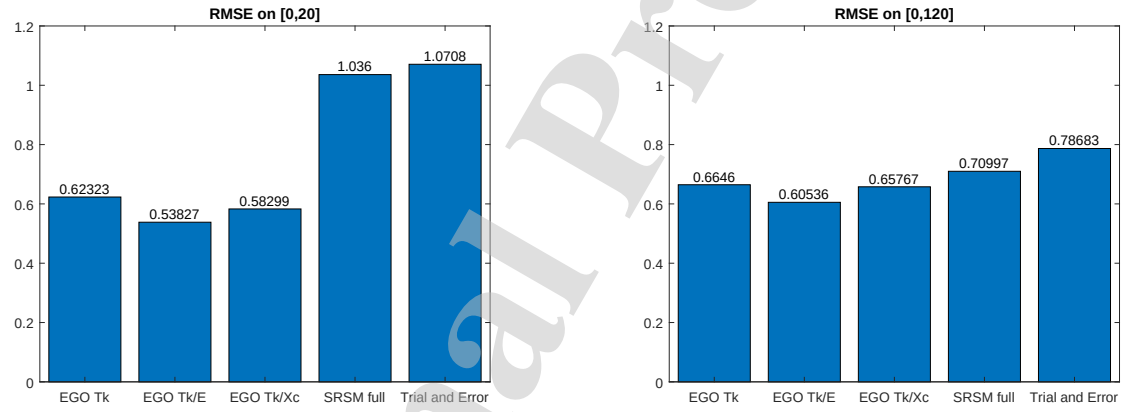

(a) (b)

Figure 21: (a) RMSE evaluated on the full crush curve; (b) RMSE Evaluated on the first 20 mm of crush displacement.

in Figure 21, which provides visual evidence of the RMSE accuracy measure for different test cases. From Figure 21a, it is evident that the optimization of the MSE objective function on the full displacements range does not provide an accurate approximation of the initial part of the curve, which is mostly influenced by the trigger definition. On the other hand, when focusing the optimization strategy to minimize the MSE computed on the first 20 mm of crush displacement only, the found optima still perform well when simulated on a total time that is sufficient to cover the full displacements range, as illustrated in Figure 21b.

In Figure 22, the load-displacement curves extracted from the experimental tests are compared to the ones resulting from the simulations that are set according to the results of the optimization procedure.

In Figure 22a, the curves resulting from the optimization studies on the trigger component are shown. It can be assessed that all the curves associated to the optimal parameter configurations returned by EGO provide a more accurate approximation of the experimental curve than the trial-end-error method. Indeed, the optimized trigger allows

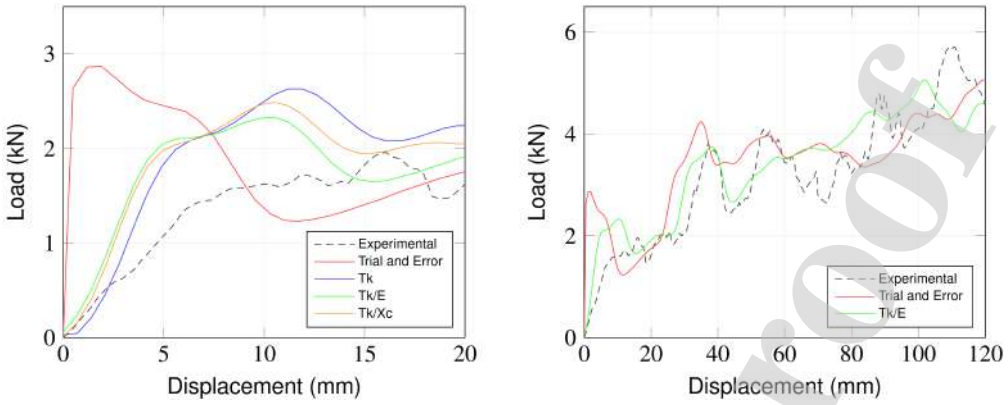

(a) (b)

Figure 22: Comparison of experimental and numerical load-displacement curves. (a) The experimental curve is compared to the optimized curves and the Trial and Error curve on the [0, 20] mm displacement range. (b) The experimental curve is compared to the best optimized curve in terms of RMSE and the Trial and Error curve on the [0, 120] mm displacement range.

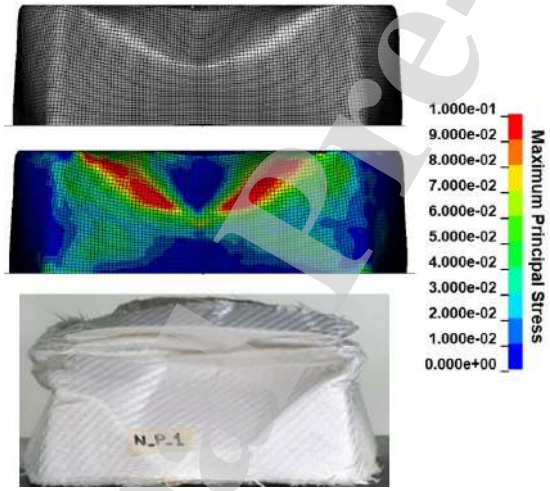

Figure 23: Crush behavior of the optimized numerical impact attenuator and comparison with the experimental test.

for attenuating the initial pick due to contact instabilities between the impacting rigid wall and the component in the numerical simulations. It is also evident that the blue curve, which is the outcome of the simulation corresponding to the solution of EGO on the one-dimensional test case, tends to overly overestimate the experimental trend if compared to the curves obtained as optima of the 2-variables test cases. In Figure 22b, the experimental and trial and error curves are compared to the numerical curve that provides the lower RMSE among all the considered test cases, i.e., the outcome of the complete simulation on the numerical model set according to the optimum of the EGO Tk/E test case. Also here, it can be noted that such a curve is able to capture the experimental behavior with satisfactory accuracy, by definitely improving the approximation provided by the numerical model tuned by hand. The first 50 mm of crushing are well approximated by the numerical curve (green) as well as the peak of force at 40 mm, that corresponds to the first thickness variation, and the following drop of load. The rest of the numerical curve follows a less scattered path respect to the experimental one, due to the absence of the compacted walls on the impacting edge of the attenuator, that causes the “up and down” force trend. However, the average increasing tendency is well

followed by the numerical curve.

Finally, Figure 23 shows the crushing behavior of the impact attenuator with optimized properties. It is noticeable that the the global deformations and the bending of the vertical face in correspondence of the thickness variation are well captured. The same cannot be said for the folding and compacting of the top edge. Indeed, the element erosion criteria of the material card lead the elements in contact with the rigid wall to be deleted before that layer compaction occurs.

7. Conclusions

In this paper, a numerical optimization study for the material parameter identification of an All-PP composite impact attenuator in crashworthiness was presented. It is well known that the mechanical properties determined by standard tests usually do not adequately reflect the failure mechanism of a composite component subjected to crush loading, especially in the case of the particular failure mode of an All-PP composite material. Therefore, the problem of scaling from specimen to component was addressed using a parameter identification procedure from LS-OPT based on the optimization of the numerical load-displacement crush curve with respect to the most influential parameters of the numerical model. In this study, an optimization methodology consisting of several conceptual building blocks was developed and tested. The optimization study is divided into two sub-problems. The first problem aims at optimizing the material card parameters based on minimizing the Mean Square Error (MSE) between the experimental and numerical load-displacement curves recorded for the whole range of displacements [0, 120] mm. Here, the parameters SOFT and DFAILc of the LS-DYNA material card were chosen as the variables to be optimized. On the other hand, the second problem has the more focused objective of optimizing both the geometrical and material parameters of a numerical trigger with degraded properties, which was modeled and optimized to represent the top edge imperfections and reduce the initial contact instabilities between the rigid wall and the impact attenuator. In this second phase, the objective was to minimize the MSE on the shorter range [0, 20] mm. The introduction of the numerical trigger and its optimization proved to be a good solution for damping the oscillations and force peaks during the first impact phases. In the logical flow of the method, two different surrogate-based optimization strategies were considered: the Sequential Response Surface Method (SRSM) and the Efficient Global Optimization (EGO) algorithms. The two strategies were compared in terms of exploitative/explorative search behavior and convergence speed towards an optimal solution. Furthermore, the paper contains a detailed description of the practical setup of the optimizers in LS-OPT. This is particularly useful in the case of EGO, which was introduced to the software relatively recently and, after a thorough search of the relevant literature, has never been applied to similar mechanical test cases. The results show that optimization is beneficial for refining significant parameters on both the full component and the trigger. The obtained numerical load-displacement curve accurately reproduces the experimental results. An improvement over the numerical curve obtained by trial and error was visible in terms of accuracy measures as well as in the visual inspection of the resulting curves. In summary, the exploratory and exploitative capabilities of the EGO algorithm make it a more convenient choice for optimizing the objective function with low computational cost.

Funding

This research did not receive any specific grant from funding agencies in the public, commercial, or not-for-profit sectors.

Data Availability

The raw/processed data required to reproduce these findings are available to download from `https://data.mendeley.com/datasets/vrctbtnswz/1`.

References

[1] Y. Wan, J. Takahashi, Development of Carbon Fiber-Reinforced Thermoplastics for Mass-Produced Automotive Applications in Japan, J Comp Sci 5 (2021) 86. doi:10.3390/jcs5030086.

[2] P. Kiss, W. Stadlbauer, C. Burgstaller, H. Stadler, S. Fehringer, F. Haeuserer, V. M. Archodoulaki, In-house recycling of carbon- and glass fibre-reinforced thermoplastic composite laminate waste into high-performance sheet materials, Composites. Part A 139 (2020). doi:10.1016/j.compositesa.2020.106110.

[3] T. A. De Bruijn, G. Vincent, F. W. Van Hattum, Recycling C/PPS laminates into long fibre thermoplastic composites by low shear mixing, ICCM Int Conf Compos Mater 2017-Augus (2017) 20–25. URL: http://www.iccm-central.org/Proceedings/ICCM21proceedings/papers/4122.pdf.

[4] R. J. Tapper, M. L. Longana, I. Hamerton, K. D. Potter, A closed-loop recycling process for discontinuous carbon fibre polyamide 6 composites, Composites, Part B 179 (2019) 107418. doi:10.1016/j.compositesb.2019.107418.

[5] D. S. Cousins, Y. Suzuki, R. E. Murray, J. R. Samaniuk, A. P. Stebner, Recycling glass fiber thermoplastic composites from wind turbine blades, J Cleaner Prod 209 (2019) 1252–1263. doi:10.1016/j.jclepro.2018.10.286.

[6] B. Liu, P. Zhu, A. Xu, L. Bao, Investigation of the recycling of continuous fiber-reinforced thermoplastics, J Thermoplast Compos Mater 32 (2019) 342–356. doi:10.1177/0892705718759388.

[7] R. Ciardiello, G. Belingardi, B. Martorana, V. Brunella, Effect Of Accelerated Ageing Cycles On The Physical And Mechanical Properties Of A Reversible Thermoplastic Adhesive, J Adhes 96 (2020) 1003–1026. doi:10.1080/00218464.2018.1553714.

[8] R. Ciardiello, G. Belingardi, F. Litterio, V. Brunella, Thermomechanical characterization of reinforced and dismountable thermoplastic adhesive joints activated by microwave and induction processes, Compos Struct 244 (2020) 112314. doi:10.1016/j.compstruct.2020.112314.

[9] M. E. Kazemi, L. Shanmugam, D. Lu, X. Wang, B. Wang, J. Yang, Mechanical properties and failure modes of hybrid fiber reinforced polymer composites with a novel liquid thermoplastic resin, Elium®, Composites, Part A 125 (2019) 105523. doi:10.1016/j.compositesa.2019.105523.

[10] S. K. Bhudolia, S. C. Joshi, Low-velocity impact response of carbon fibre composites with novel liquid Methylmethacrylate thermoplastic matrix, Compos Struct 203 (2018) 696–708. doi:10.1016/j.compstruct.2018.07.066.

[11] S. K. Bhudolia, S. C. Joshi, A. Bert, B. Yi Di, R. Makam, G. Gohel, Flexural characteristics of novel carbon methylmethacrylate composites, Compos Commun 13 (2019) 129–133. doi:10.1016/j.coco.2019.04.007.

[12] S. K. Bhudolia, G. Gohel, K. F. Leong, S. C. Joshi, Damping, impact and flexural performance of novel carbon/Elium® thermoplastic tubular composites, Composites, Part B 203 (2020). doi:10.1016/j.compositesb.2020.108480.

[13] M. E. Kazemi, L. Shanmugam, Z. Li, R. Ma, L. Yang, J. Yang, Low-velocity impact behaviors of a fully thermoplastic composite laminate fabricated with an innovative acrylic resin, Compos Struct 250 (2020). doi:10.1016/j.compstruct.2020.112604.

[14] I. Y. Chang, J. K. Lees, Recent Development in Thermoplastic Composites: A Review of Matrix Systems and Processing Methods, J Thermoplast Compos Mater 1 (1988) 277–296. doi:10.1177/089270578800100305.

[15] H. Ning, N. Lu, A. A. Hassen, K. Chawla, M. Selim, S. Pillay, A review of Long fibre thermoplastic (LFT) composites, Int Mater Rev 65 (2020) 164–188. doi:10.1080/09506608.2019.1585004.

[16] L. Di Landro, W. Lorenzi, Mechanical properties and dynamic mechanical analysis of thermoplastic-natural fiber/glass reinforced composites, Macromol Symp 286 (2009) 145–155. doi:10.1002/masy.200951218.

[17] S. Boria, A. Scattina, G. Belingardi, Axial energy absorption of CFRP truncated cones, Compos Struct 130 (2015) 18–28. doi:10.1016/j.compstruct.2015.04.026.

[18] J. Obradovic, S. Boria, G. Belingardi, Lightweight design and crash analysis of composite frontal impact energy absorbing structures, Compos Struct 94 (2012) 423–430. doi:10.1016/j.compstruct.2011.08.005.

[19] T. Matsuo, M. Kan, K. Furukawa, T. Sumiyama, H. Enomoto, K. Sakaguchi, Numerical modeling and analysis for axial compressive crushing of randomly oriented thermoplastic composite tubes based on the out-of-plane damage mechanism, Compos Struct 181 (2017) 368–378. doi:10.1016/j.compstruct.2017.08.104.

[20] S. Boria, A. Scattina, G. Belingardi, Experimental evaluation of a fully recyclable thermoplastic composite, Compos Struct 140 (2016) 21–35. doi:10.1016/j.compstruct.2015.12.049.

[21] W. Tan, B. G. Falzon, Modelling the crush behaviour of thermoplastic composites, Compos Sci Technol 134 (2016) 57–71. doi:10.1016/j.compscitech.2016.07.015.

[22] S. Dong, A. Sheldon, K. Carney, Modeling of Carbon-Fiber-Reinforced Polymer (CFRP) Composites in LS-DYNA ® with Optimization of Material and Failure Parameters in LS-OPT ®, 15th Int LS-Dyna Users Conf (2018). URL: https://api.semanticscholar.org/CorpusID:201819486.

[23] A. Vujović, Z. Krivokapić, R. Grujičić, J. Jovanović, A. Pavlović, Combining FEM and neural networking in the design of optimization of traditional Montenegrin chair, FME Trans 44 (2016) 374–379. doi:10.5937/fmet1604374V.

[24] P. Beaumont, C. Soutis, A. Hodzic, Structural Integrity and Durability of Advanced Composites | Scribd, Woodhead Publishing - Elsevier, Cambridge, UK, 2015. doi:10.1016/C2014-0-01469-4.

[25] J. Wang, N. Yang, J. Zhao, D. Wang, Y. Wang, K. Li, Z. He, B. Wang, Design and experimental verification of composite impact attenuator for racing vehicles, Compos Struct 141 (2016) 39–49. doi:10.1016/j.compstruct.2016.01.013.

[26] S. Boria, J. Obradović, G. Belingardi, On design optimization of a composite impact attenuator under dynamic axial crushing, FME Trans 45 (2017) 435–440. doi:10.5937/fmet1703435B.

[27] J. M. P. B. C. Castro, M. Fontana, A. L. Araujo, J. F. A. Madeira, Optimization of a composite impact attenuator for a formula student car, Mech Adv Mater Struc (2020) 1–11. doi:10.1080/15376494.2020.1712627, publisher: Taylor & Francis.

[28] A. Ciampaglia, D. Fiumarella, C. Boursier Niutta, R. Ciardiello, G. Belingardi, Impact response of an origami-shaped composite crash box: Experimental analysis and numerical optimization, Compos Struct 256 (2021) 113093. doi:10.1016/j.compstruct.2020.113093.

[29] N. Stander, A. Basudhar, W. Roux, K. Witowski, T. Eggleston, T. Goel, K. Craig, LS-OPT® User's Manual, A Design Optimiza-

tion and Probabilistic Analysis Tool for the Engineering Analyst, Livermore Software Technology Corporation, 2019. URL: https://www.lsoptsupport.com/documents/manuals.

[30] E. Raponi, M. Bujny, M. Olhofer, N. Aulig, S. Boria, F. Duddeck, Kriging-guided Level Set Method for Crash Topology Optimization, in: 7th GACM Colloquium on Computational Mechanics for Young Scientists from Academia and Industry, Stuttgart, Germany, 2017. URL: https://api.semanticscholar.org/CorpusID:65485843.

[31] E. Raponi, M. Bujny, M. Olhofer, N. Aulig, S. Boria, F. Duddeck, Kriging-assisted topology optimization of crash structures, Comput Methods Appl Mech Eng 348 (2019) 730–752. doi:10.1016/j.cma.2019.02.002.

[32] A. I. J. Forrester, A. Sóbester, A. J. Keane, Engineering Design via Surrogate Modelling - A Practical Guide, John Wiley & Sons Ltd., 2008. doi:10.1002/9780470770801.

[33] N. Stander, K. Craig, On the robustness of a simple domain reduction scheme for simulation-based optimization, Eng Comput 19 (2002) 431–450. doi:10.1108/02644400210430190.

[34] D. R. Jones, M. Schonlau, W. J. Welch, Efficient Global Optimization of Expensive Black-Box Functions, J Global Optim 13 (1998) 455–492. doi:10.1023/A:1008306431147.

[35] S. Boria, G. Belingardi, D. Fiumarella, A. Scattina, Experimental crushing analysis of thermoplastic and hybrid composites, Comp Struct 226 (2019) 111241. doi:10.1016/j.compstruct.2019.111241.

[36] S. Boria, G. Belingardi, A. Scattina, Thermosetting and thermoplastic impact attenuator under axial loading, Multiscale and Multidiscip Model, Exp Des 2 (2019) 129–139. doi:10.1007/s41939-018-0037-5.

[37] E. Raponi, D. Fiumarella, Experimental analysis and numerical optimization of a thermoplastic composite in crashworthiness, IOP Conf Ser: Mater Sci Eng 1038 (2021) 012030. doi:10.1088/1757-899X/1038/1/012030.

[38] S. Boria, A. Scattina, Energy absorption capability of laminated plates made of fully thermoplastic composite, P I Mech Eng C-J Mec 232 (2018) 1389–1401. doi:10.1177/0954406218760059.

[39] D. Fiumarella, S. Boria, G. Belingardi, A. Scattina, Experimental characterization and finite element modelling of a thermoplastic composite lamina subjected to large shear deformation, Mater Des Process Commun 3 (2021) e156. doi:10.1002/mdp2.156.

[40] F. Libonati, L. Vergani, Damage assessment of composite materials by means of thermographic analyses, Composites, Part B 50 (2013) 82–90. doi:10.1016/j.compositesb.2013.01.012.

[41] P. Feraboli, B. Wade, F. Deleo, M. Rassaian, M. Higgins, A. Byar, LS-DYNA MAT54 modeling of the axial crushing of a composite tape sinusoidal specimen, Composites, Part A 42 (2011) 1809–1825. doi:10.1016/j.compositesa.2011.08.004.

[42] F.-K. Chang, K.-Y. Chang, A Progressive Damage Model for Laminated Composites Containing Stress Concentrations, J Compos Mater 21 (1987) 834–855. doi:10.1177/002199838702100904.

[43] D. C. Montgomery, Design and Analysis of Experiments, 8th Edition, John Wiley & Sons, Incorporated, 2012. URL: https://books.google.de/books?id=XQAcAAAAQBAJ.

[44] J. H. Holland, Adaptation in Natural and Artificial Systems: An Introductory Analysis with Applications to Biology, Control and Artificial Intelligence, MIT Press, Cambridge, MA, USA, 1992. URL: https://ieeexplore.ieee.org/servlet/opac?bknumber=6267401.

E-ail:elena.raponi@unicam.it

EditorofJournalCompositeStructures

Object:CRediT(ContributorRolesTaxonomy)

Paris,August2nd,2021

DearEditor,

Herearesynthetizedtheindividualauthorcontributions:

- ElenaRaponi:Conceptualization,Methodology,Investigation,Datacuration,Validation,Visualization,Writing-originaldraft,Writing-Review&Editing.
- DarioFiumarella:Conceptualization,Software,Investigation,Datacuration,Validation,Visualization,Writing-originaldraft,Writing-Review&Editing.
- SimonettaBoria:Conceptualization,Supervision,Investigation,Writing-Review&Editing.
- AlessandroScattina:Conceptualization,Supervision,Investigation,Writing-Review&Editing.
- GiovanniBelingardi:Conceptualization,Supervision,Resources,Writing-Review&Editing.

Yourssincerely,

Theauthors

Declaration of interests

☒ The authors declare that they have no known competing financial interests or personal relationships that could have appeared to influence the work reported in this paper.

☐The authors declare the following financial interests/personal relationships which may be considered as potential competing interests: